Soft Matter

Cite this: *Soft Matter*, 2012, **8**, 3163

www.rsc.org/softmatter

PAPER

Self-assembly of crystalline–coil diblock copolymers in solution: experimental phase map

Adriana M. Mihut,*[a] Jérôme J. Crassous,[a] Holger Schmalz,[b] Markus Drechsler[b] and Matthias Ballauff[c]

Received 19th July 2011, Accepted 12th December 2011
DOI: 10.1039/c2sm06359j

We present the morphological phase map of semicrystalline poly(butadiene)-*b*-poly(ethylene oxide) (PB-*b*-PEO) diblock copolymers (BCP) in dilute *n*-heptane solutions. The solutions of the diblock copolymer have been quenched from 70 °C, that is above the melting temperature T_m of the PEO block, following two thermal pathways: (A) by direct immersion into liquid nitrogen and (B) by quenching to the crystallization temperature T_c of the PEO block. Scanning force microscopy (SFM) and transmission electron microscopy (TEM) allowed imaging of the dried crystalline morphologies, whereas in solution the micelles have been visualized by cryogenic transmission electron microscopy (cryo-TEM). The apparent hydrodynamic radii of the micellar structures in solution were determined by dynamic light scattering (DLS). The effects of the block length and block ratio, and the influence of the thermal history on the morphology have been systematically investigated for the series of PB-*b*-PEO BCP. In pathway A, different morphologies such as spheres, rods, worms and entangled cylinders have been observed; whereas in pathway B, as the weight fraction and the length of the PEO block increased, the morphology changed from spherical to cylindrical or to lamellar, and finally to large dendritic micelles. This tailoring of morphologies is fully reversible with temperature and was found to correlate to the crystalline state of the PEO chains.

1 Introduction

The ability of amphiphilic block copolymers to self-assemble into well-ordered nanostructures in selective solvents has attracted significant interest over the past few years. This is due to the convenient size and shape tunability of the structures obtained by simply changing their molecular weights and compositions.[1,2] Thus, block copolymers (BCP) dissolved in selective solvents can associate to form micelles in which the insoluble polymer block forms the micelle core and the soluble block the corona. In addition to the classic morphologies of spheres[3] and wormlike micelles (cylinders)[4–7] a large variety of geometries such as vesicles,[8–11] discs,[12] toroids,[12–14] Janus structures,[15] nanotubes,[16,17] helices,[18,19] bowl-shaped[20] and raspberry-like micelles[21] can be obtained from BCP by self- assembly.

More recently a lot of attention has been paid to the self-assembly of block copolymers in selective solvents, where one of the blocks can crystallize. The crystallization affects the self-assembled nanostructures and creates unique and interesting morphologies.[22–35] The resulting morphologies can be viewed as sandwich-like structures consisting of chain-folded crystalline core domains coated with swollen amorphous layers.[36–39] It has been reported that alteration of the block copolymers composition, concentration and solvent selectivity leads to different crystalline morphologies like spheres or spherical aggregates,[40–42] cylinders (depending on their flexibility, these structures are refereed to as rod-like or worm-like micelles),[22–29] and lamellar structures.[30,37,43]

Morphological transitions can be induced not only by variation of the block lengths but also by a change of solvent quality.[17,27] Winnik and co-workers reported structures of PFS-*b*-PDMS block copolymer under varying solvent conditions.[17] Moreover, these authors have shown that PFS block copolymers can generate micellar architectures such as block co-micelles by epitaxial growth from the ends of the crystalline cores of cylindrical micelles or the edges of platelets.[30] Xu and co-workers demonstrated that the micellar morphologies formed by PCL-*b*-PEO block copolymers in aqueous medium depend on the length of the crystalline PCL block.[27]

We have previously shown that a symmetric poly(butadiene)-*b*-poly(ethylene oxide) (PB-*b*-PEO) BCP forms crystalline-core micelles of different morphologies such as spheres, meanders (branched lamellae) and twisted lamellae by judicious choice of

[a]*Adolphe Merkle Institute, University Fribourg, Route de l'Ancienne Papeterie, PO Box 209, 1723 Marly 1, Switzerland. E-mail: adriana.mihut@unifr.ch; Fax: +41263009624; Tel: +41263009123*
[b]*Macromolecular Chemistry II, University Bayreuth, D-95440 Bayreuth, Germany*
[c]*Soft Matter and Functional Materials, Helmholtz-Zentrum Berlin für Materialien und Energie GmbH, Glienicker Strasse 100, 14109 Berlin, Department of Physics, Humboldt University Berlin, Newtonstr. 15, 12489 Berlin, Germany*

the crystallization temperature.[44,45] A detailed investigation of the crystals development through micellar aggregation demonstrated that the nucleation and growth of the micellar PEO core (*e.g.* homo/heterogeneous process) determines the resulting morphology.[45] Manipulating not only the crystallization conditions but also the solvent quality for the amorphous PB corona chains by lowering the temperature leads to the transition from a spherical to a rod-like morphology. This was explained by a change of the spontaneous curvature due to the less demanding packing of the corona chains in a poorer solvent. In addition, the interplay between a micelles aggregation and crystallization led to a time-dependent reorganization in the micellar system and a transition from rod-like to needle-like micelles was observed.[46] Thus, these studies have shown that PB-*b*-PEO block copolymers in *n*-heptane are an excellent model system for the investigation of crystalline micellar morphologies,[44–46] in addition to the well-established non-crystalline micellar phases of PB-*b*-PEO block copolymers in water (a selective solvent for PEO).[5,47]

In this paper we extend previous studies[44–46] in order to explore the full parameter space and to establish the phase map of the BCP under various conditions and for a wide range of molecular weights and block ratios. The morphologies were generated from hot polymer solutions (above the T_m of the PEO block) *via* two routes: by immersion into liquid nitrogen (Pathway A) and by quenching to the crystallization temperature of the PEO block (Pathway B). We have previously shown that $B_{88}EO_{12}^{29.5}$ and $B_{52}EO_{48}^{5.6}$ diblock copolymers self-assemble to form micelles with a crystalline PEO core.[44–46] The data of $B_{88}EO_{12}^{29.5}$ and $B_{52}EO_{48}^{5.6}$ samples reported in our former studies[44–46] were employed here to complete the micellar phase map. This paper is organized as follows: the first part outlines the semicrystalline micellar morphologies obtained *via* the two thermal crystallization pathways. In the following, different relevant parameters that play a major role in the self-assembly process and enable the formation of well-defined structures such as crystallization temperature, the effect of solvent solubility and the influence of the BCPs molecular composition on micellar morphologies are discussed. Finally, we describe the experimental crystalline morphology map for PB-*b*-PEO BCPs in *n*-heptane.

2 Experimental

Materials

The polybutadiene-*block*-poly(ethylene oxide) diblock copolymers with a composition given by $B_xEO_y^M$ were purchased from Polymer Source Inc.[48,49] The subscripts denote the mass fraction in percent of the corresponding PB (x), PEO (y) blocks and the superscript gives the overall number average molecular weight M_n of the BCPs in kg mol^{-1}. Molecular characteristics of the diblock copolymers such as the number average molecular weights M_{PB} and M_{PEO}, the polydispersity index (PDI), the weight fraction of the PEO blocks w_{PEO} and the degree of polymerization of PB and PEO blocks, N_{PB} and N_{PEO}, respectively are listed in Table 1. The crystallization/melting temperatures (T_c/T_m) in the bulk samples determined by DSC are summarized as well. The $B_{52}EO_{48}^{5.6}$ diblock copolymer was synthesized *via* sequential anionic polymerization as described in a previous study.[44] The samples prepared from 1 wt% *n*-heptane solutions were first kept at 70 °C for 30 min and then quenched *via* the two pathways. If lower concentrations were required, the 1 wt% stock solutions were diluted accordingly.

Scanning force microscopy (SFM)

The SFM experiments were performed using a Dimension 3100M microscope (Veeco Instruments) equipped with a Nanoscope software operated in TappingMode at room temperature. The samples were prepared by spin-coating the 0.1 wt% *n*-heptane solutions onto freshly cleaned silicon wafers. Scan rates between 0.5–1.0 Hz were used. The crystalline PEO block is much stiffer then the amorphous PB block which allowed us to use an imaging mode based on a higher phase shift in the phase contrast images, that is complementary to the topographic imaging mode.

Transmission electron microscopy (TEM)

Samples were prepared by placing a drop of the polymer solution (0.1 wt% in *n*-heptane) on a carbon-coated copper grid. After a few seconds, excess solution was removed by blotting with filter paper. Staining was performed with osmium tetroxide (OsO_4) vapor for 60 s. OsO_4 is known to selectively stain PB, *i.e.*, PB domains are expected to appear darker compared to PEO domains, which enables us to distinguish between the two polymers. Subsequently, bright-field TEM was performed on a Zeiss CEM 902 operating at 80 kV.

Cryogenic transmission electron microscopy (cryo-TEM) and selected area electron diffraction (SAED)

The samples were prepared by adding a 2 μl droplet of a 1 wt% polymer solutions in *n*-heptane on a lacey carbon coated copper grid. The specimens were prepared by vitrification in liquid nitrogen and then cooled to approximately 77 K in a temperature controlled freezing unit (Zeiss Cryobox, Zeiss NTS GmbH, Oberkochen, Germany). After freezing the specimen was placed into a cryo-transfer holder (CT 3500, Gatan, München, Germany) and transferred to a Zeiss 922 OMEGA EFTEM (Zeiss NTS GmbH, Oberkochen, Germany). Due to the fact that the contrast provided by the electron-density differences between the BCP and the solvent is very low, the shock-frozen *n*-heptane was sublimated when heated *in situ* at 163 K for 15 min. After the sublimation of *n*-heptane, the structures could be identified on the supporting "lacey" carbon membrane. Subsequently, the sample was cooled to a temperature of 97 K for image recording. The TEM was operated at an acceleration voltage of 200 kV. SAED measurements were carried out under the same conditions as the cryo-TEM investigations.

X-Ray diffraction (XRD)

The X-ray diffraction data were collected with Cu-K_α radiation (0.154 nm) on a Bragg–Brentano-type diffractometer (Panalytical XPERT-PRO) equipped with a X' Celerator Scientific RTMS detector. The XRD patterns were recorded in the 2θ range from 10 to 40°. All the patterns were taken from 1 wt% $B_xEO_y^M$ solutions dried at room temperature on glass slides. WAXS experiments on the polymer solutions were carried out at

Table 1 Molecular characteristics of the diblock copolymers and thermal properties of the bulk samples

Polymer	M_{PB}	M_{PEO}	M_n	PDI	w_{PEO}	T_c	T_m	N_{PEO}	N_{PB}/N_{PEO}
$B_{88}EO_{12}^{29.5}$	26.0	3.5	29.5	1.06	0.12	−30	52	80	6.01
$B_{80}EO_{20}^{14.7}$	11.8	2.9	14.7	1.09	0.2	−27	45	66	3.32
$B_{78}EO_{22}^{33.5}$	26.0	7.5	33.5	1.06	0.22	−19	57	170	2.83
$B_{68}EO_{32}^{7.3}$	5.0	2.3	7.3	1.06	0.32	30	47	52	1.79
$B_{62}EO_{38}^{10.4}$	6.5	3.9	10.4	1.10	0.38	25	48	89	1.35
$B_{53}EO_{47}^{10.5}$	5.5	5.0	10.5	1.05	0.47	43	60	114	0.89
$B_{52}EO_{48}^{5.6}$	2.9	2.7	5.6	1.02	0.48	32	47	61	0.88
$B_{42}EO_{58}^{13.7}$	5.7	8.0	13.7	1.05	0.58	37	51	182	0.58
$B_{31}EO_{69}^{11.3}$	3.5	7.8	11.3	1.08	0.69	50	62	177	0.37

the ID2 beam lime at the European Synchrotron Radiation Facilities (ESRF, Grenoble, France). The operating wavelength of the X-ray was $\lambda = 0.1$ nm. A Linkam THMS600 temperature controller system was used as a sample holder.

Dynamic light scattering (DLS)

The experiments were carried out on an ALV-5000 compact goniometer system equipped with a He–Ne laser ($\lambda = 632.8$ nm). All measurements were performed on 0.1 wt% solutions of $B_xEO_y^M$ in *n*-heptane at a scattering angle of 90°, where the resulting apparent hydrodynamic radius was determined *via* the Stokes–Einstein relation.

3 Results and discussion

3.1 Influence of thermal pathways and geometrical confinement on morphological features

The different micellar morphologies have been generated from the hot polymer solutions (70 °C) *via* two thermal pathways: (A) by direct immersion into liquid nitrogen, where *n* -heptane becomes a poor solvent for both blocks at very low temperatures, and (B) by quenching to the crystallization temperature T_c of the PEO block (see Table 1). While at 70 °C the BCPs self-assembled into micellar structures consisting of a molten PEO core and a soluble PB corona, cooling the polymer solutions at temperatures lower than T_m the PEO block crystallizes in the micellar core. In this pathway *n*-heptane is a poor solvent only for the PEO block.

3.2 Pathway A: self-assembly at low crystallization temperature

Fig. 1 shows the SFM phase contrast images of the morphologies formed by $B_xEO_y^M$ block copolymers *via* pathway A in *n*-heptane. The micellar cores, composed of the crystalline PEO block, appear as bright areas, whereas the darker areas represent the micellar PB corona. Our previous *in situ* time-resolved WAXS investigations revealed that crystallization of the PEO block takes place in solution upon quenching to very low temperatures.[44] Hereby, the micellar structures are fixed by crystallization in solution before the freezing point of the *n*-heptane solvent, that is at −91 °C. Once the solvent is frozen no further rearrangement of the micelles can occur.[44,45]

As the PEO block content increases (w_{PEO}), a sequence of structural elements was documented beginning with rod-like micelles (R), then spheres (S) and then cylinders, named worm-like micelles (W). Increasing the core weight fraction further leads to an additional structural element, referred as entangled cylinders (EC). Moreover, we noted here that this morphological sequence was separated by composition windows containing mixed morphologies, as S + R and S + W.

The PB-*b*-PEO BCPs with w_{PEO} between 20% and 48% formed S micelles in *n*-heptane with dimensions ranging from 25 nm to 43.5 nm. An overlap of R and S micelles is observed for the $B_{62}EO_{38}^{10.4}$ BCP with a weight fraction of $w_{PEO} = 0.38$ (Fig. 1(E)). In this coexistence region, R micelles with lengths of 78 ± 7 nm and diameters of 26 ± 3 nm were frequently observed. By increasing the weight fraction of the PEO block a transition from S to C micelles was observed. The increased PEO composition to $w_{PEO} = 0.58$, is manifested in the dominance of W micelles over S micelles as shown in Fig. 1(H).

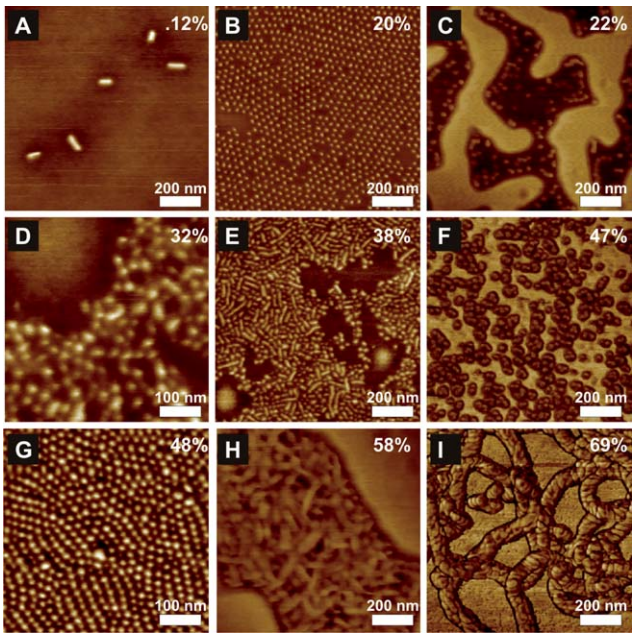

Fig. 1 Pathway A: SFM phase contrast images of crystalline micellar morphologies of $B_xEO_y^M$ block copolymers in *n*-heptane after immersion into liquid nitrogen of the 0.1 wt% polymer solutions from 70 °C: (A) $B_{88}EO_{12}^{29.5}$: rods; (B) $B_{80}EO_{20}^{14.7}$: spheres; (C) $B_{78}EO_{22}^{33.5}$: spheres; (D) $B_{68}EO_{32}^{7.3}$: spheres; (E) $B_{62}EO_{38}^{10.4}$: rods and spheres; (F) $B_{53}EO_{47}^{10.5}$: spheres; (G) $B_{52}EO_{48}^{5.6}$: spheres; (H) $B_{42}EO_{58}^{13.7}$: worms and spheres; and (I) $B_{31}EO_{69}^{11.3}$: entangled cylinders. The weight fraction of the PEO block is indicated for guidance.

An unusual feature was observed for $B_{31}EO_{69}^{11.3}$ BCP (w_{PEO} = 0.69). This new morphological state referred as entangled cylinder (EC), has not been observed in PB-*b*-PEO diblocks or any other linear system where one block is able to crystallizes in a micellar core. These EC micelles have an average width of 81 ± 9 nm with a height of 32 nm. The structure of the core more closely resembles that of a ribbon-like structure. We could not obtain an average length due to the limited size of the images; however, lengths in excess of 5 μm were observed. Examination of large area images shows the formation of a network with a random interconnection of the cylinders.

The molecular characteristics of these BCPs, and the micelles morphologies as determined by SFM are listed in Table 2. Moreover, the hydrodynamic radii R_H of the micelles with swollen PB chains in *n*-heptane determined by DLS measurements are summarized in Table 2.

Our results seem coherent with previous work in which we have shown that two PB-*b*-PEO BCPs such as $B_{88}EO_{12}^{29.5}$ (w_{PEO} = 0.12) and $B_{52}EO_{48}^{5.6}$ (w_{PEO} = 0.48) can self-assemble to form R and S micelles, respectively, with a crystalline PEO core and a PB corona in *n*-heptane.[44,46]

Aggregation number. When the dimension of the core in the micelles is known, we can estimate the aggregation number (that is, the number of polymer chains forming the core) and the area occupied per PB block from the density of the PEO block.[41] Fig. 2 displays representative TEM images of S micelles obtained *via* pathway A. Imaging of the micellar core was possible after staining the samples with osmium tetroxide, which reacts only with the PB chains. The PEO core diameters varied from 12 to 20 nm as the PEO block weight fractions increased.

Assuming that the density of the crystalline micelles is the same as the crystalline bulk density (ρ_{PEO} = 1.239 g cm^{-3}), the aggregation number N_{agg} of the chains forming the crystalline micelles is calculated using the following equation:

$$N_{agg} = \frac{4/3\pi R_{PEO}^3 \rho_{PEO}}{M_{PEO}} \times 6.02 \times 10^{23} \quad (1)$$

Subsequently, the area occupied per PB block (S) is given as:

$$S = \frac{4\pi R_{PEO}^2}{N_{agg}} \quad (2)$$

Fig. 2A displays the estimated aggregation number N_{agg} and the area occupied per PB block (S) of the S micelles formed by $B_xEO_y^M$ diblock copolymers in *n*-heptane. Hereby, the aggregation number N_{agg} increases with the weight fraction w_{PEO} of the PEO block, whereas the area occupied per PB block decreases (S). The hydrodynamic radii R_H of the S micelles with swollen PB chains in *n*-heptane determined by DLS measurements and the corresponding PEO core radii evaluated from the TEM micrographs are illustrated in (Fig. 2B).

It is important to point out that, the crystalline micelles generated *via* pathway A though a fast quenching in liquid nitrogen mostly retained the micellar morphology present in the molten state at 70 °C of the PB-*b*-PEO BCPs with weight fractions 0.2 < w_{PEO} ≤ 0.48.

3.3 Pathway B: self-assembly at the crystallization temperature of the PEO block

Fig. 3 shows the SFM images of the morphologies obtained by direct quenching of the hot solutions to the crystallization temperature T_c of the PEO block for the bulk samples (Pathway B; see Table 1 and Table 2). The following morphologies were identified with increasing PEO weight fraction (w_{PEO}) in the PB-*b*-PEO BCPs: spheres (S), cylinders (C), platelets (P), lamellae (L) or branched lamellae (BL) and dendrites (D). Mixed morphologies such as platelets with cylindrical micelles (P + C) and of platelets with lamellar morphologies (P + L) were also identified.

S micelles were obtained at smaller weight fractions of PEO (w_{PEO} ≤ 0.32) in the copolymers (Fig. 3(A–C)), whereas an increase of the w_{PEO} to 32% and 38% allowed the formation of square P structures (Fig. 3(D)). Moreover, coexistence of P + C and of P + L morphologies were observed at w_{PEO} = 0.38 (Fig. 3(E)) and w_{PEO} = 0.47 (Fig. 3(F)), respectively. Recently, we reported that at w_{PEO} = 0.48, the $B_{52}EO_{48}^{5.6}$ BCP self-assembles into BL, namely a meander-like structure (Fig. 3(G)).[44,45] Increasing the w_{PEO} content to 0.58 and 0.69, results in a morphological transition from BL to P (Fig. 3(H)) and to D structures (Fig. 3(I)), respectively.

Fig. 4 summarizes the morphological behavior of the $B_xEO_y^M$ BCPs upon cooling at the crystallization temperature T_c. It is found that the T_c of BCPs increases with w_{PEO}. We also notice that the BCPs with a small PEO content such as $B_{88}EO_{12}^{29.5}$,

Table 2 Micellar sizes of $B_xEO_y^M$ block copolymers. The apparent hydrodynamic diameter D_H measured by DLS and the average sizes D^{SFM} measured by SFM at room temperature are summarized. In the case of the non-spherical morphologies, the notations [a] and [b] indicate the length and the width of the structures, respectively. The observed basic morphologies are spheres (S), rods (R), worms (W), cylinders (C), entangled cylinders (EC), lamellae (L), branched lamellae (BL), platelets (P) and dendrites (D)

	Pathway A			Pathway B		
Polymer	Morph	D_H^{DLS}	D^{SFM}	Morph	D_H^{DLS}	D^{SFM}
$B_{88}EO_{12}^{29.5}$	R	77	90 ± 20[a], 40 ± 8[b]	S	63	45.5 ± 4
$B_{80}EO_{20}^{14.7}$	S	44	34 ± 3	S	46	33.5 ± 4
$B_{78}EO_{22}^{33.5}$	S	73	39 ± 5	S	69	42 ± 5
$B_{68}EO_{32}^{7.3}$	S	53	42 ± 5	P	—	5500 ± 4000
$B_{62}EO_{38}^{10.4}$	S, R	178	78 ± 7[a], 26 ± 3[b] (R)	C, P	—	35 ± 2[b] (C), 5750 ± 2000 (P)
$B_{53}EO_{47}^{10.5}$	S	46	43.55 ± 5	L, P	—	107 ± 27[b] (L), 204 ± 50 (P)
$B_{52}EO_{48}^{5.6}$	S	36	25 ± 2	BL	230	40 ± 4[b]
$B_{42}EO_{58}^{13.7}$	S, W	56	50 ± 10[a], 26 ± 4[b] (W)	P	—	372 ± 96[a], 280 ± 70[b]
$B_{31}EO_{69}^{11.3}$	EC	—	128 ± 24[b]	D	—	81 ± 8[b]

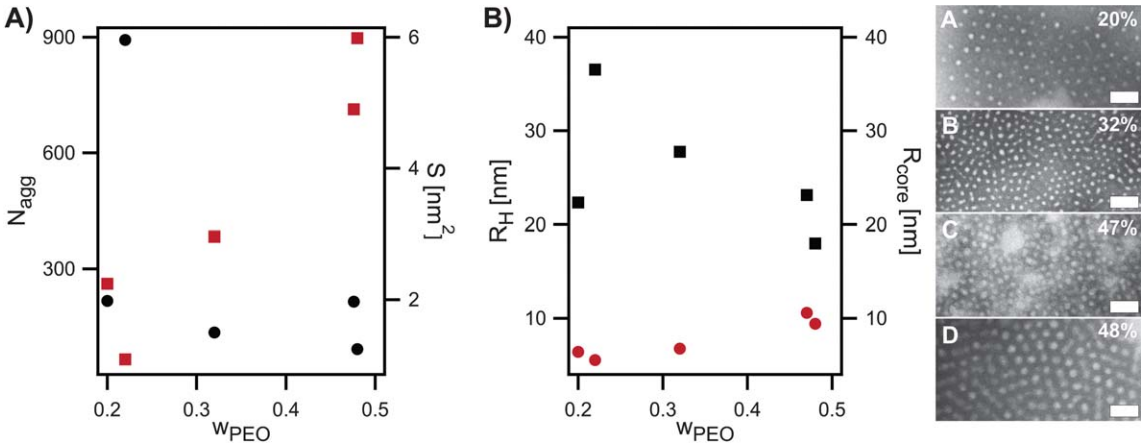

Fig. 2 A) The aggregation number, N_{agg} (red squares), and the area occupied per PB block, S (black circles) as a function of the PEO block weight fraction. B) Hydrodynamic radius (black squares) of the spherical micelles and PEO core radius (red circles) evaluated from the stained TEM micrographs as a function of the weight fraction of the PEO block. TEM micrographs of spherical block copolymer micelles formed in *n*-heptane by: (A) $B_{80}EO_{20}^{14.7}$ ($w_{PEO} = 0.20$); (B) $B_{68}EO_{32}^{7.3}$ ($w_{PEO} = 0.32$); (C) $B_{53}EO_{47}^{10.5}$ ($w_{PEO} = 0.47$); (D) $B_{52}EO_{48}^{5.6}$ ($w_{PEO} = 0.48$). Osmium tetroxide was used as staining agent to improve the contrast. The scale bars are 200 nm.

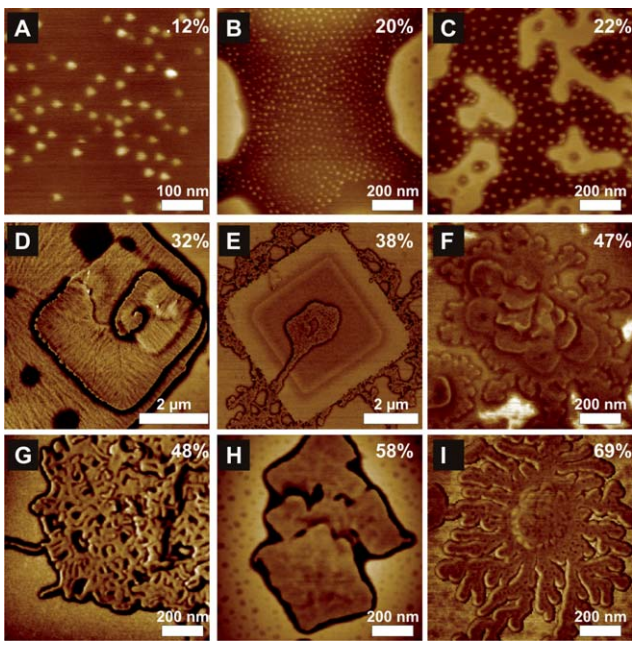

Fig. 3 Pathway B: SFM phase contrast images of crystalline morphologies formed in *n*-heptane at the crystallization temperature of the PEO block (0.1 wt% polymer solutions): (A) $B_{88}EO_{12}^{29.5}$: spheres; (B) $B_{80}EO_{20}^{14.7}$: spheres; (C) $B_{78}EO_{22}^{33.5}$: spheres; (D) $B_{68}EO_{32}^{7.3}$: platelets; (E) $B_{62}EO_{38}^{10.4}$: coexistence of cylinders and platelets; (F) $B_{53}EO_{47}^{10.5}$: coexistence of lamellae and platelets; (G) $B_{52}EO_{48}^{5.6}$: meanders (branched lamellae); (H) $B_{42}EO_{58}^{13.7}$: platelets and (I) $B_{31}EO_{69}^{11.3}$: dendrite-like structures. The weight fraction of the PEO block is indicated for guidance.

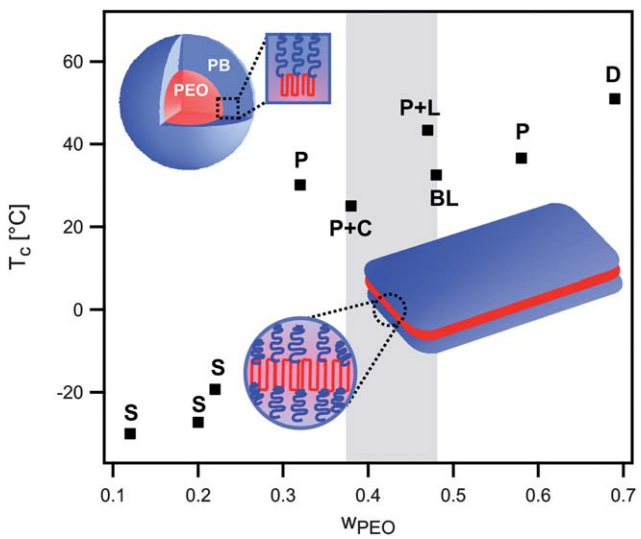

Fig. 4 Experimentally determined correlation between the crystallization temperature (T_c) and the molecular composition (w_{PEO}) of the trend in morphology obtained for the $B_xEO_y^M$ block copolymers *via* Pathway B: spheres (S), platelets (P), platelets + cylinders (P + C), platelets + lamellae (P + L), branched lamellae (BL) and dendrites (D). Coexistent phases were observed in the ranges between $w_{PEO} = 0.38$–0.47.

$B_{80}EO_{20}^{14.7}$ and $B_{78}EO_{22}^{33.5}$ have a very low T_c (see Table 1). These BCPs fall into the temperature range where homogeneous nucleation is normally observed.[50] As a result, these BCPs formed S micelles upon cooling, indicating that crystallization is confined within the original BCP morphology present in the molten state. Otherwise, crystallization breaks out the original BCP morphology allowing secondary nucleation of crystallization to proceed from domain to domain, forming L or P structures as the PEO composition increases gradually, *i.e.*, for higher T_c (see Table 1). There is published evidence for bulk BCPs and polymer blends, that the crystallization temperature is a good indicator of the crystallization behavior, that is confinement or breakout.[51,52] The results shown here demonstrate that T_c stands as well as a general indicator for the crystallization behavior of BCPs in solution.

Scaling models for coil–crystalline polymers in solution provide us with a theoretical framework to aid in understanding these results.[38,39] Despite confinement, the crystallization of

polymer chains follows the conventional habit; whereby polymer chains fold back and forth into stems to form crystalline lamellae, that is, the micellar core with a thickness of ≅10 to 20 nm. In this case, the free energy of the crystalline-core BCP micelles, consists of three parts: the enthalpy of fusion of the crystalline block, the conformational entropy of the amorphous block, and the interfacial energy. The balance between the interfacial energy between the solvent and the core surface, and the stretching within the swollen coils of the corona seems to be the major factor which determines the micellar geometry. Moreover, for BCPs with longer amorphous blocks, the entropy of the amorphous block has a larger contribution to the total free energy, where the amorphous block is densely packed rather then highly stretched.[39] The densely packed amorphous block protects the lateral interface from interaction with the solvent and hinders the aggregation of the BCP micelles, which explains the formation of structures of high curvature, *i.e.* spherical micelles rather then lamellar micelles tend to be formed at lower content of the PEO block. Furthermore, all these components are dependent on the chain folding of the crystalline block.

Dimension of the crystals

Due to the complexity of the crystalline morphologies, an important parameter that can influence the self-assembly mechanism such as the chain folding will be discussed in the following. In order to understand how the chain folding evolves with the length of the PEO block, the average overall thickness (H) of the lamellar structures formed by the $B_xEO_y^M$ BCPs has been determined from the SFM images.

Fig. 5 shows the thickness evolution with the weight fraction of the PEO block. To calculate the thickness of the crystalline PEO lamellae, the first assumption we made is that the density of the PEO block is identical to that of the crystalline bulk density ($\rho_{PEO} = 1.239$ g cm^{-3}), where that of the amorphous PB block is $\rho_{PB} = 0.884$ g cm^{-3}. The micellar platelets appear as a crystalline-core grafted with solvent-swollen corona at both sides.[37,39] The lamellar thickness (H) is the sum of the corona thickness (d_{PB}) and the core thickness (d_{PEO}), *i.e.*, $H = 2d_{PB} + d_{PEO}$. The d_{PEO} values were calculated for the lamellar morphologies formed though the pathway B at w_{PEO} varying between 0.32 and 0.69 (Fig. 5) by using the expression:

$$d_{PEO} = H\frac{M_{PEO}/\rho_{PEO}}{M_{PEO}/\rho_{PEO} + M_{PB}/\rho_{PB}} \quad (3)$$

where ρ_{PEO}, ρ_{PB} and M_{PEO}, M_{PB} are the density and the number average molecular weight of the PEO and PB blocks, respectively. Moreover, the thickness of the core is determined by the number of folds, n_f and the length of the crystallizable block:

$$d_{PEO} = \frac{L_{PEO}}{n_f + 1} \quad (4)$$

where L_{PEO} is the length of the unfolded PEO block with a helical conformation, $L_{PEO} = 0.2783N_{PEO}$ with a repeating unit of 0.2783 nm.[53–55] The estimated fold numbers are plotted in Fig. 5 as a function of the PEO block weight fraction w_{PEO}.

One has to take into account that, the n_f is limited by the length of the PEO block. In this case, the behavior of the $B_{53}EO_{47}^{10.5}$ ($w_{PEO} = 0.47$) and $B_{52}EO_{48}^{5.6}$ ($w_{PEO} = 0.48$) BCPs at T_c were compared. In the $B_{53}EO_{47}^{10.5}$ and $B_{52}EO_{48}^{5.6}$ BCPs, the fully extended chains of PEO with a helical conformation are 31.72 nm and 16.97 nm in length, respectively. The PEO block is folded twice in the $B_{53}EO_{47}^{10.5}$ ($N_{PEO} = 114$) BCP, whereas in the smaller $B_{52}EO_{48}^{5.6}$ ($N_{PEO} = 61$) BCP exhibits only one fold. Consequently, more defined platelets are expected for the $B_{53}EO_{47}^{10.5}$ BCP (see Fig. 3(F)). Thus, the number of folds of the crystalline block n_f was seen to increase with increasing the weight fraction w_{PEO} and the degree of polymerization of the PEO block, N_{PEO}. Also, a large number of folds n_f, leads to strong repulsions and to a sharp interface between the crystalline PEO core and the solvent-swollen PB corona, which in turn favors smaller lamellar thickness, d_{PEO}. Moreover, as the n_f increased, the core curvatures decreased and the lateral growth of the crystals was enlarged. In this case, the lamellae thickness is governed by a balance between an entropic contribution due to the stretching of solvated chains and an enthalpic contribution due of folding of crystalline chains in the lamellae.

Thus, the crystallite dimensions and its expected shape of a series of PB-*b*-PEO BCPs in *n*-heptane matches well with the theoretical predictions for the micellar geometry of

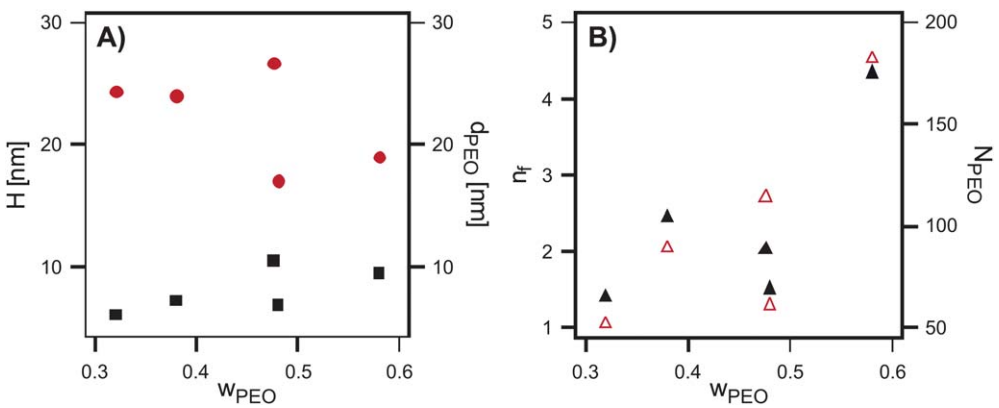

Fig. 5 A) Overall average thickness (H, red circles) of the $B_xEO_y^M$ lamellar micelles determined from the SFM images and calculated PEO crystallite size (d_{PEO}, black squares) as a function of the PEO block weight fraction. B) Number of chain folds for the PEO block (n_f, black full triangles) in the lamellar crystallite and the degree of polymerization of the PEO (N_{PEO}, red hollow triangles) as a function of the PEO block weight fraction.

semicrystalline BCPs in a selective solvent.[39] By increasing the length and the weight fraction of the crystalline block (therefore, the T_c), the folding number of PEO increases, and thus the area occupied by each PB chain becomes larger, leading to the decrease in the grafting density of the PB chains, and the S micelles are transformed into C or L structures. Moreover, to the best of our knowledge, this is the first detailed investigation done on semicrystalline micelles of PB-*b*-PEO BCPs in the selective solvent, *n*-heptane.

Morphological coexistence. The detailed discussion of the structure in the coexistence regions and the comparison between the morphologies formed upon cooling *via* the two thermal pathways, at identical w_{PEO} composition, will be given in context of the TEM results (Fig. 6). Selective staining of the samples with osmium tetroxide, which reacts only with the PB chains, generated a characteristic contrast between the two polymers confirming that the PB chains (dark areas) constitute the corona of the micellar morphologies.

R and S micelles are formed by the $B_{62}EO_{38}^{10.4}$ BCP (w_{PEO} = 0.38) after quenching in liquid nitrogen. In this case, we can conclude that the micellar morphology present in the molten state was mainly retained *via* Pathway A, as DLS indicated at 70 °C, the presence of micelles with a R_H of 98 nm. However, when crystallization occurs at T_c = 25 °C (Pathway B) this BCP self-assembles into C micelles that coexist with P structures (Fig. 6(A–B)).

Crystallization at T_c yielded morphological transitions from S micelles to an L structure at weight fractions of 47 and 48%, respectively. The $B_{53}EO_{47}^{10.5}$ BCP self-assembled into L and P structures (Fig. 6D), whereas the $B_{52}EO_{48}^{5.6}$ BCP formed BL reported as meanders (Fig. 6F).[44,45] Hereby, Pathway A retained the S melt morphology. Our earlier studies confirmed that at T_c, crystallization-induced aggregation of S micelles present in the molten state occurs and leads to L structure formation of the $B_{52}EO_{48}^{5.6}$ BCP.[44,45] The W micelles formed at $w_{PEO} \geq 0.58$ are retained after immersion into liquid nitrogen, whereas Pathway B leads to the formation of square P (Fig. 6(H)) and D structure (Fig. 6(J)).

Hence, it is demonstrated that by changing only the crystallization temperature, we can access a wide diversity of reversible micelles without changing the composition of the system (see Fig. 9). Note that one PB-*b*-PEO BCP generates two distinct morphologies, *e.g.*, spheres (S)–platelets (P), rods (R)–platelets (P), spheres (S)–branched lamellae (BL), worms (W)–platelets (P) or entangled cylinders (EC)–dendrites (D). The whole process is reversible as soon as the solutions are heated again to 70 °C, that is, above the T_m of the PEO blocks. No changes were recorded when selected solutions were examined a few months after preparation. The dimensions of the structures determined by TEM are consistent with the results obtained from SFM (see Table 2).

3.4 Insights into the crystalline nature of the morphologies

To determine the crystal structure of the micellar PEO core X-ray diffraction experiments were carried out. The XRD patterns highlight the crystalline nature of the dried morphologies; whereas, WAXS measurements were performed on the polymer

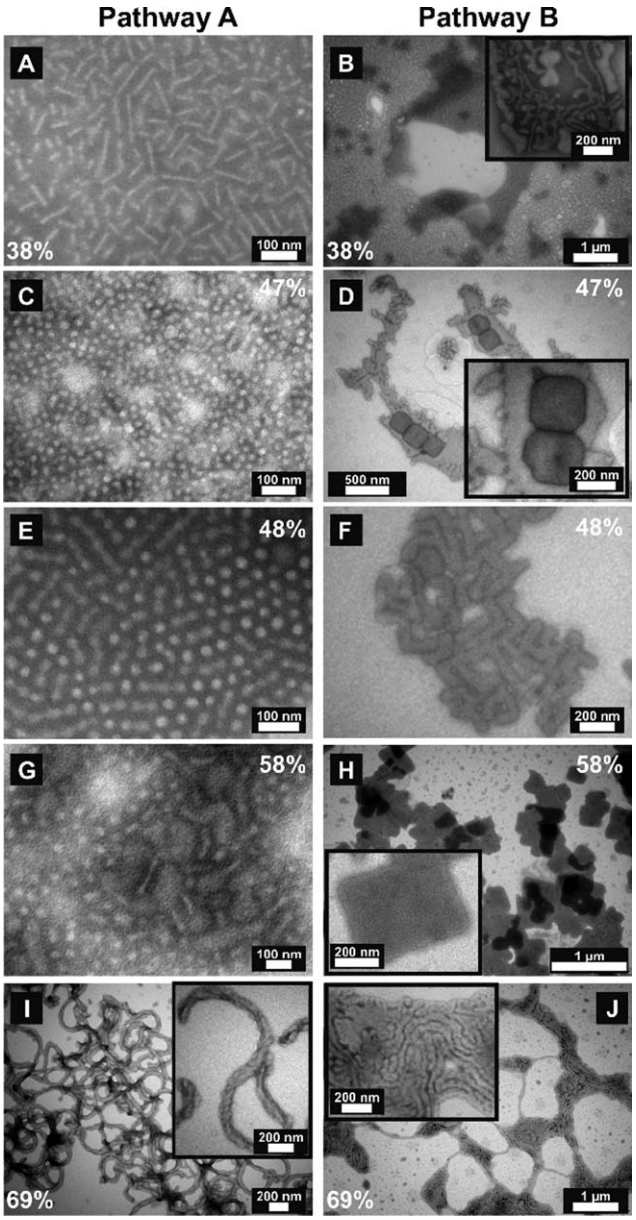

Fig. 6 TEM micrographs of morphologies of the $B_xEO_y^M$ block copolymers in *n*-heptane formed by Pathways A and B: $B_{62}EO_{38}^{10.4}$: coexistence of rods and spheres (A); coexistence of cylinders and platelets (B); $B_{53}EO_{47}^{10.5}$: spheres (C); coexistence of lamellae and platelets (D); $B_{52}EO_{48}^{5.6}$: spheres (E); branched lamellae (F); $B_{42}EO_{58}^{13.7}$: spheres and worms (G); platelets (H); $B_{31}EO_{69}^{11.3}$: entangled cylinders (I); dendrites (J). The weight fraction of the PEO block is indicated for guidance.

solutions.[44] Representative XRD results are presented in Fig. 7, representing patterns of the films prepared from 1wt% copolymer solutions of $B_{80}EO_{20}^{14.7}$ and $B_{31}EO_{69}^{11.3}$, which form S, EC, and D, respectively. The XRD peaks which appear at 2θ = 19°, 23°, are assigned to the (120) and (032 + 112) reflections of polyethylene oxide crystallized in its monoclinic modification.[56] Only the $B_{88}EO_{12}^{29.5}$ diblock copolymer shows a triclinic modification of the PEO block.[46,57]

The degree of crystallinity (X_c) was estimated from the XRD patterns, as the ratio between the areas below the crystalline

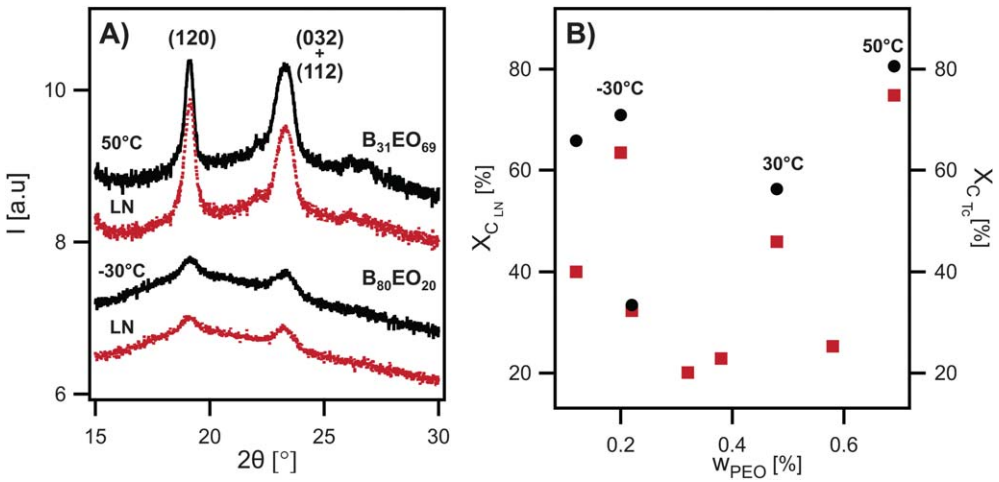

Fig. 7 A) XRD patterns of films of 1wt% $B_{80}EO_{20}^{14.7}$ and $B_{31}EO_{69}^{11.3}$ polymer solutions in *n*-heptane. The red lines indicate the diffraction patterns of the BCP morphologies formed by Pathway A: spheres ($B_{80}EO_{20}^{14.7}$) and entangled cylinders ($B_{31}EO_{69}^{11.3}$); whereas, the black lines represent the diffraction patterns of the morphologies formed by Pathway B: spheres ($B_{80}EO_{20}^{14.7}$, $T_c = -30$ °C) and dendrites ($B_{31}EO_{69}^{11.3}$, $T_c = 50$ °C). The XRD patterns were shifted along the ordinate for a better visualization. The diffraction patterns are attributed to (120) and (032 + 112) PEO reflections. B) Degree of crystallinity in dependence on the morphologies formed by: Pathway A ($X_{c,LN}$, red squares) and pathway B (X_{c,T_c}, black circles).

Bragg peaks to the total scattered area and the weight fraction of the PEO block in the block copolymer.[58] As emphasized in Fig. 7A) w_{PEO} is the major parameter that affects X_c of the structures besides the thermal history of the polymers solutions. As the w_{PEO} in the BCP increases, the crystallinity degree X_{c,T_c} shifts to higher values when the morphology varied from S to L structures (Pathway B). The maximum crystallinity values were reached at the highest PEO content (Fig. 7B). The same trend was observed in the $X_{c,LN}$ when the polymer solutions are quenched into liquid nitrogen (Pathway A). Variations in X_c were observed between the morphologies formed through Pathway A ($X_{c,LN}$) and B (X_{c,T_c}), respectively at identical w_{PEO} content (Fig. 7B). According to these results, the crystallinity is dependent on the crystallization kinetics of the PEO block and the mechanism of crystal growth, that is, confined crystallization or breakout crystallization. It has to be noted that at T_c, the crystals are no longer confined to the microdomains in which they nucleate, followed by growth and rearrangements/recrystallization into larger structures accompanied by an increase in the crystallinity (see Fig. 6), whereas at lower temperatures confined crystallization occurs independent in each micellar PEO core preserving the melt structure (see Fig. 1). Our previous *in situ* time-resolved WAXS investigations on the $B_{52}EO_{48}^{5.6}$ BCP revealed that the meander morphology formed *via* Pathway B at $T_c = 30$ °C, had a higher X_c compared with the S micelles obtained though Pathway A (see Fig. 7).[44]

Fig. 8 shows the P morphologies grown in solution from the $B_{68}EO_{32}^{7.3}$ (A) and $B_{62}EO_{38}^{10.4}$ (C) BCPs (Pathway B), where the samples were prepared by *in situ* freeze-drying cryo-TEM as described elsewhere.[44] To probe the crystallinity of the P structures, selected area electron diffraction (SAED) was carried out under cryogenic conditions. The four strong diffraction spots visualized in the SAED patterns were attributed to the (120) plane of the monoclinic PEO crystals (Fig. 8B,D), confirming the investigation by XRD on dried samples and by WAXS in solution (see Fig. 7). These results assert that the crystallization took place in solution and was not subsequent to the drying of the BCPs.

Generality of the method. The diagram in Fig. 9 summarizes the obtained PB-*b*-PEO crystalline morphologies in *n*-heptane as a function of molecular size and composition, where N_{PEO} and w_{PEO} are the degree of polymerization and weight fraction of the PEO blocks, respectively. This representation describes the tendency of the micelles (present in the molten state at 70 °C) to reorganizes at different crystallization conditions. A common feature in the crystallization behavior is observed for these

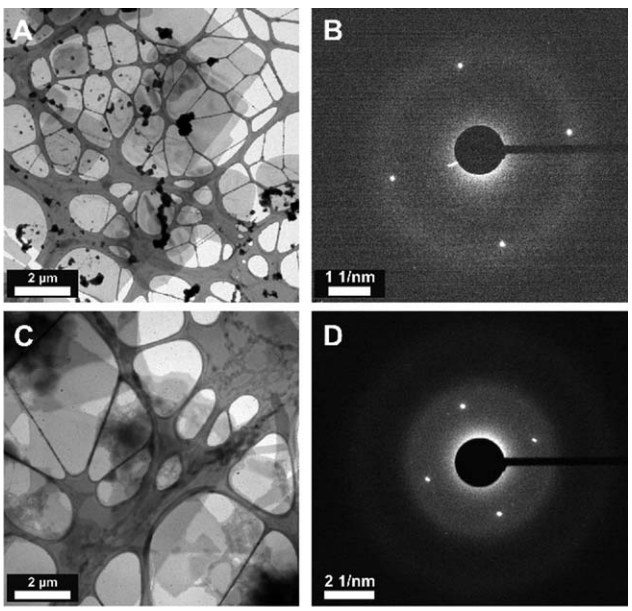

Fig. 8 Cryo-TEM micrographs and SAED images of the P structures formed by the $B_{68}EO_{32}^{7.3}$ (A–B) and $B_{62}EO_{38}^{10.4}$ (C–D) diblock copolymers. The diffraction patterns are attributed to (120) PEO reflections.

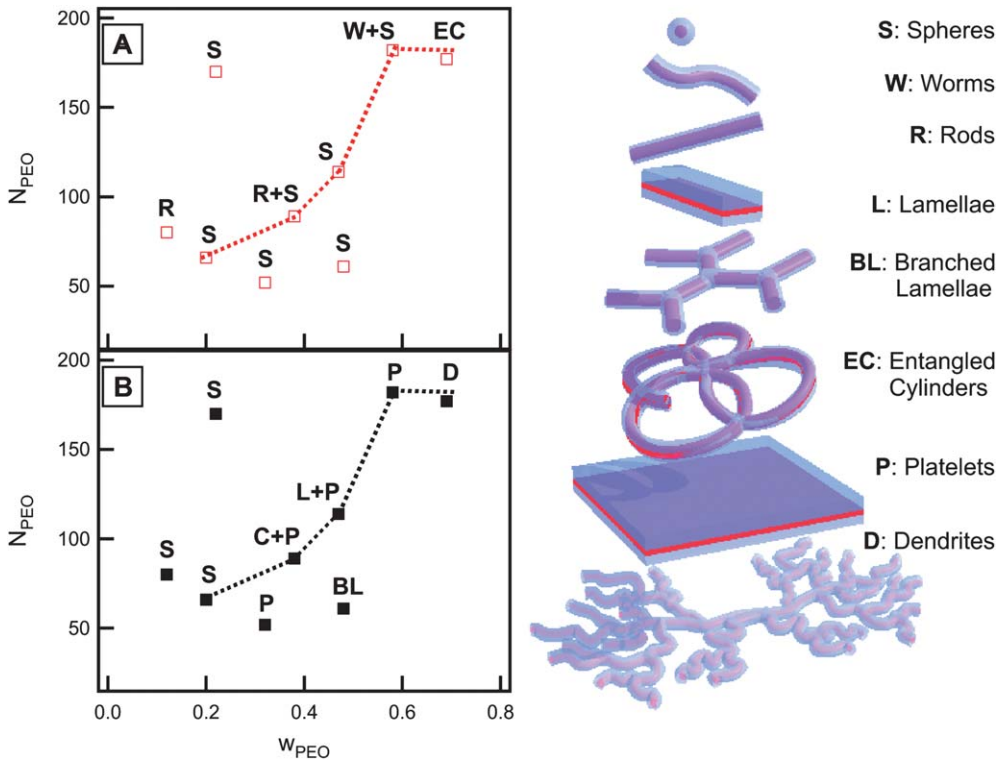

Fig. 9 Crystalline morphology diagram for PB-*b*-PEO in *n*-heptane as a function of molecular size and composition, where N_{PEO} and w_{PEO} are the degree of polymerization and weight fraction of the PEO block, respectively. A) Two basic morphologies—spheres (S) and cylinders (referred as rods (R), worms (W) and entangled cylinders (EC))—were formed by immersion into liquid nitrogen (Pathway A). Mixed populations of rods + spheres (R + S) and worms + spheres (W + S) were observed. B) At the crystallization temperature T_c of the PEO block (Pathway B) spheres (S), lamellae (L) or branched lamellae (BL), platelets (P) and dendrites (D) formed in the solutions as the PEO block composition increases. Mixed populations of cylinders + platelets (C + P) and lamellae + platelets (L + P) were observed. The dashed lines establish the morphological trend of the PB-*b*-PEO block copolymers at similar molecular weights, M_n.

diblock copolymers. As crystallization takes place at low temperatures (Pathway A) the spherical morphology is mostly retained at compositions of the PEO block ≤0.58, *i.e.*, the crystallization of the PEO block occurred and was effectively confined within the micellar core without introducing any obvious perturbation to the micellar structure. In consequence the morphology of the micelles with molten PEO cores (that is, at 70 °C) was almost unperturbed.

A break-out from the spherical morphology present at 70 °C (molten PEO core) occurs upon crystallization at the T_c of the PEO block (Pathway B) above $w_{PEO} = 0.32$. Here, transitions from spheres to lamellar morphologies are observed. The worm-like micelles obtained at PEO composition above 58% were retained upon quenching into liquid nitrogen, whereas Pathway B leads to larger morphologies as platelets and dendrites, respectively. Moreover, at equal composition of the PEO and PB block, crystallization induced aggregation of the spherical units of the melt, favoring the development of branched lamellae (BL, meanders),[44] platelets (P), and lamellae with platelets (L + P). An exception occurred at $w_{PEO} = 0.12$, where rod-like micelles were formed *via* Pathway A, whereas Pathway B retained the spherical shape present in the molten state.[46]

In addition to the thermal history and the weight fraction w_{PEO}, the length of the crystallizable PEO block had an influence on the micellar morphology. It can be seen that an increase in the PEO block content yielded morphological transitions from spheres to lamellae or platelet-like structures. Therefore, the lengths of the PEO and PB blocks had an important effect on the micellar morphology (see Fig. 9, dashed lines).

The present results can hence be qualitatively compared to data obtained by Jain and Bates,[5] for the PB-*b*-PEO morphologies in water, a poor solvent for the PB blocks. Even if, the PEO block is not crystallizing in water, the self-assembly behavior of the PB-*b*-PEO BCPs in selective solvents, *i.e.*, water and *n*-heptane, followed a similar trend. These authors reported that S micelles are formed at high PEO weight fraction, whereas morphological transitions to cylinders or bilayers are observed with the decrease of the PEO block fraction. Mixed morphologies like spheres with cylinders, or cylinders with bilayers appeared to coexist in a broad overlapping range between 0.40 and 0.60. In our study, we observed that both thermal pathways, favor the coexistence of crystalline morphologies in the broad range 0.38–0.58. Phenomena of morphological coexistence are believed to occur as a consequence of the polydispersity in chain lengths, which allows assembly in more than one aggregate geometry.[47] Hereby, crystallization is the main driving force that dominates the morphological evolution and favors coexistence regions along with the block lengths variation.

4 Conclusion

We reported the first morphological phase map of semicrystalline PB-*b*-PEO diblock copolymer micelles in the selective solvent *n*-heptane. A series of diblocks with different compositions and molecular weights have been investigated. The micelles consisting of a crystalline PEO core and a soluble PB corona were generated from hot polymer solution *via* two crystallization pathways, that is: by undercooling to the temperature of liquid nitrogen (Pathway A) and by cooling to the crystallization temperature T_c of the PEO blocks (Pathway B). Two complete phase portraits were established, corresponding to these thermal pathways. At very low crystallization temperature (Pathway A) the sequence of spheres, rods, worms and entangled cylinders was observed, whereas at T_c (Pathway B) the micellar morphology changed progressively from spheres to cylinders, to platelets, to lamellae or branched lamellae (meanders) and to dendrites with increasing weight fraction of the PEO, w_{PEO}. In addition to these features, coexisting regions of rods + spheres, worms + spheres for Pathway A and platelets + cylinders, platelets + lamellae for Pathway B appeared in a broad range of BCP compositions ($0.38 \leq w_{PEO} \leq 0.58$).

SFM was employed to quantify the overall size of the micelles and to estimate the thickness of the crystalline PEO core, whereas the TEM investigations led to direct determination of the length scales of the PEO core/PB corona domains. X-Ray measurements indicated that as the structure evolves from spheres to lamellae there is a significant increase in the degree of crystallinity of the PEO-cores; w_{PEO} being the major parameter that affects the crystallinity of the structures.

This approach confirms that controlled crystallization of BCPs in a selective solvent can be an efficient way to generate complex and yet unseen morphologies giving rise to an entire new class of diblock copolymer materials. In addition, such self-assembly process has the advantage to be fully reversible, once the polymer solutions are heated above the melting temperature of the crystalline block, the system recovers its original amorphous state.

Acknowledgements

A.M.M. acknowledge the financial support from the European Community's "Marie-Curie Actions" under Contract No. MRTN-CT-2004-504052 [POLYFILM] and from the Adolphe Merkle Foundation. Financial support by the Deutsche Forschungsgemeinsschaft, SFB 840 - project A2, Bayreuth, is gratefully acknowledged. The authors thank Michael Möller for the XRD investigations. We thank Dr Emanuela Di Cola for assistance with the WAXS experiments at ESRF.

References

1 R. C. Hayward and D. J. Pochan, *Macromolecules*, 2010, **43**, 3577–3584.
2 T. Smart, H. Lomas, M. Massignani, M. V. Flores-Merino, L. R. Perez and G. Battaglia, *Nano Today*, 2008, **3**, 38–46.
3 J. F. Gory, *Adv. Polym. Sci.*, 2005, **190**, 65–136.
4 P. Bhargava, J. X. Zheng, P. Li, R. P. Quirk, F. W. Harris and S. Z. D. Cheng, *Macromolecules*, 2006, **39**, 4880–4888.
5 S. Jain and F. S. Bates, *Science*, 2003, **300**, 460–464.
6 Y.-Y. Won, H. T. Davis and F. S. Bates, *Science*, 1999, **283**, 960–963.
7 Z. Li, E. Kesselman, Y. Talmon, M. A. Hillmyer and T. P. Lodge, *Science*, 2004, **306**, 98–101.
8 D. E. Discher and A. Eisenberg, *Science*, 2002, **297**, 967–973.
9 G. Battaglia and A. J. Ryan, *J. Am. Chem. Soc.*, 2005, **127**, 8757–8764.
10 J. Zhu, N. Ferrerb and R. C. Hayward, *Soft Matter*, 2009, **5**, 2471–2478.
11 J. Zhu and R. C. Hayward, *Angew. Chem., Int. Ed.*, 2008, **47**, 2113–2116.
12 H. Cui, Z. Chen, K. L. Wooley and D. J. Pochan, *Macromolecules*, 2006, **39**, 6599–6607.
13 D. J. Pochan, Z. Chen, H. Cui, K. Hales, K. Qi and K. L. Wooley, *Science*, 2004, **306**, 94–97.
14 J. Zhu, Y. Liao and W. Jiang, *Langmuir*, 2004, **20**, 3809–3812.
15 A. Walther and A. H. E. Müller, *Soft Matter*, 2008, **4**, 663–668.
16 K. Yu, L. Zhang and A. Eisenberg, *Langmuir*, 1996, **12**, 5980–5984.
17 J. Raez, I. Manners and M. A. Winnik, *J. Am. Chem. Soc.*, 2002, **124**, 10381–10395.
18 S. Zhong, H. Cui, Z. Chen, K. L. Wooley and D. J. Pochan, *Soft Matter*, 2008, **4**, 90–93.
19 J. J. L. M. Cornelissen, M. Fischer, N. A. J. M. Sommerdijk and R. J. M. Nolte, *Science*, 1998, **280**, 1427–1430.
20 I. C. Riegel, A. Eisenberg, C. L. Petzhold and D. Samios, *Langmuir*, 2002, **18**, 3358–3363.
21 S. Kubowicz, J.-F. Baussard, J.-F. Lutz, A. F. Thünemann, H. von Berlepsch and A. Laschewsky, *Angew. Chem., Int. Ed.*, 2005, **44**, 5262–5265.
22 J. A. Massey, K. Temple, L. Cao, Y. Rharbi, J. Raez, M. A. Winnik and I. Manners, *J. Am. Chem. Soc.*, 2000, **122**, 11577–11584.
23 L. Shen, H. Wang, G. Guerin, C. Wu, I. Manners and M. Winnik, *Macromolecules*, 2008, **41**, 4380–4389.
24 J. Raez, J. P. Tomba, I. Manners and M. A. Winnik, *J. Am. Chem. Soc.*, 2003, **125**, 9546–9547.
25 J. Raez, I. Manners and M. A. Winnik, *Langmuir*, 2002, **18**, 7229–7239.
26 X. Wang, H. Wang, D. J. Frankowski, P. G. Lam, P. M. Welch, M. A. Winnik, J. Hartmann, I. Manners and R. J. Spontak, *Adv. Mater.*, 2007, **19**, 2279–2285.
27 Z.-X. Du, J.-T. Xu and Z.-Q. Fan, *Macromolecules*, 2007, **40**, 7633–7637.
28 H. Schmalz, J. Schmelz, M. Drechsler, J. Yuan, A. Walther, K. Schweimer and A. M. Mihut, *Macromolecules*, 2008, **41**, 3235–3242.
29 M. Lazzari, D. Scalarone, C. Vazquez-Vazquez and M. A. Lopez-Quintela, *Macromol. Rapid Commun.*, 2008, **29**, 352–357.
30 T. Gädt, N. S. Ieong, G. Cambridge, M. A. Winnik and I. Manners, *Nat. Mater.*, 2009, **8**, 144–150.
31 J. B. Gilroy, T. Gädt, G. R. Whittell, L. Chabanne, J. M. Mitchels, R. M. Richardson, M. A. Winnik and I. Manners, *Nat. Chem.*, 2010, **2**, 566–570.
32 A. P. Soto, J. B. Gilroy, M. A. Winnik and I. Manners, *Angew. Chem., Int. Ed.*, 2010, **49**, 8220–8223.
33 S.-C. Chen, G. Wu, J. Shi and Y.-Z. Wang, *Chem. Commun.*, 2011, **47**, 4198–4200.
34 L. Yin and M. A. Hillmyer, *Macromolecules*, 2011, **44**, 3021–3028.
35 T. Gädt, F. H. Schacher, N. McGrath, M. A. Winnik and I. Manners, *Macromolecules*, 2011, **44**, 3777–3786.
36 B. Lotz and A. J. Kovacs, *Kolloid. Z. Z. Polym.*, 1966, **209**, 97–114.
37 B. Lotz, A. J. Kovacs, G. A. Bassett and A. Keller, *Kolloid. Z. Z. Polym.*, 1966, **209**, 115–128.
38 E. K. Lin and A. P. Gast, *Macromolecules*, 1996, **29**, 4432–4441.
39 T. Vilgis and A. Halperin, *Macromolecules*, 1991, **24**, 2090–2095.
40 D. Richter, D. Schneiders, M. Monkenbusch, L. Willner, L. J. Fetters, J. S. Huang, M. Lin, K. Mortensen and B. Farago, *Macromolecules*, 1997, **30**, 1053–1068.
41 J. T. Xu, J. P. A. Fairclough, S. M. Mai and A. J. Ryan, *J. Mater. Chem.*, 2003, **13**, 2740–2748.
42 J. Fu, B. Luan, X. Yu, Y. Cong, J. Li, C. Pan, Y. Han, Y. Yang and B. Li, *Macromolecules*, 2004, **37**, 976–986.
43 Z. X. Du, J. T. Xu and Z. Q. Fan, *Macromol. Rapid Commun.*, 2008, **29**, 467–471.
44 A. M. Mihut, A. Chiche, M. Drechsler, H. Schmalz, E. D. Cola, G. Krausch and M. Ballauff, *Soft Matter*, 2009, **5**, 208–213.
45 A. M. Mihut, J. J. Crassous, H. Schmalz and M. Ballauff, *Colloid Polym. Sci.*, 2010, **288**, 573–578.
46 A. M. Mihut, M. Drechsler, M. Möller and M. Ballauff, *Macromol. Rapid Commun.*, 2009, **31**, 449–453.
47 S. Jain and F. S. Bates, *Macromolecules*, 2004, **37**, 1511–1523.

48 S. Fröster and E. Krämer, *Macromolecules*, 1999, **32**, 2783–2785.
49 M. A. Hillmyer and F. S. Bates, *Macromolecules*, 1996, **29**, 6994–7002.
50 G. Reiter, G. Castelein and J.-U. Sommer, *Phys. Rev. Lett.*, 2001, **87**, 226101–1.
51 J. T. Xu, J. P. A. Fairclough, S. M. Mai, C. Chaibundit, M. Mingvanish, C. Booth and A. J. Ryan, *Polymer*, 2003, **44**, 6843–6850.
52 J. T. Xu, W. Jin, G. D. Liang and Z. Q. Fan, *Polymer*, 2005, **46**, 1709–1716.
53 A. Kovacs and C. Straupe, *J. Cryst. Growth*, 1980, **48**, 210–226.
54 J. Arlie, P. Spegt and A. Skoulios, *Makromol. Chem.*, 1967, **104**, 212–229.
55 A. J. Kovacs and A. Gonthier, *Kolloid. Z. Z. Polym.*, 1972, **250**, 530–551.
56 H. Tadokoro, Y. Chatani, T. Yoshihara, S. Tahara and S. Murahashi, *Makromol. Chem.*, 1964, **73**, 109–127.
57 Y. Takahashi, I. Sumita and H. Tadokoro, *J. Polym. Sci., Part B: Polym. Phys.*, 1973, **11**, 2113–2122.
58 G. Vonk, *J. Appl. Crystallogr.*, 1973, **6**, 148–152.